1-1-2019

Interpenetration isomers in isoreticular amine-tagged zinc MOFs

Afsaneh Khansari
University of Wollongong, afsaneh@uow.edu.au

Macguire R. Bryant
University of Wollongong, macguire@uow.edu.au

Daniel Jenkinson
University of Wollongong

Geoffrey B. Jameson
Massey University

Omid Qazvini
Massey University

See next page for additional authors

Publication Details Citation

Khansari, A., Bryant, M. R., Jenkinson, D., Jameson, G. B., Qazvini, O., Liu, L., Burrows, A. D., Telfer, S., & Richardson, C. (2019). Interpenetration isomers in isoreticular amine-tagged zinc MOFs. Faculty of Science, Medicine and Health - Papers: Part B. Retrieved from https://ro.uow.edu.au/smhpapers1/1091

Interpenetration isomers in isoreticular amine-tagged zinc MOFs

Abstract

2019 The Royal Society of Chemistry. The effect of increasing steric size of pendant amine substituents on structural isoreticulation has been studied systematically in a series of Zn-MOFs. Linear biphenyl dicarboxylic acids tagged with pendant primary amine (H2bpdc-NH2), allylamine (H2bpdc-NHallyl), diallylamine (H2bpdc-N(allyl)2) and dimethylamine (H2bpdc-NMe2) groups react with zinc nitrate in DMF to yield a set of interpenetrated MOFs, WUF-11-14, respectively, that are structurally akin to IRMOF-9. The allylated amine ligands undergo C-N cleavage reactions under the synthesis conditions, yielding WUF-12 and WUF-13 as multivariate MOFs. The single crystal X-ray crystallography on this set of MOFs was not straightforward and we give a salutary account of the difficulties encountered. Gas adsorption measurements combined with surface area calculations provide invaluable support for the crystallographic assignments. The crystallographic analyses reveal subtle differences in the relative positions of the interpenetrating frameworks, and we present a classification system for this type of MOF and analyse related examples available in the literature. CO2 adsorption measurements revealed that WUF-14, which features the strongest Brønsted basic dimethylamine tag group, has the highest capacity, isosteric heat of adsorption, and CO2/N2 selectivity.

Publication Details

Khansari, A., Bryant, M., Jenkinson, D., Jameson, G., Qazvini, O., Liu, L., Burrows, A., Telfer, S. & Richardson, C. (2019). Interpenetration isomers in isoreticular amine-tagged zinc MOFs. CrystEngComm, 21 (48), 7498-7506.

Authors

Afsaneh Khansari, Macguire R. Bryant, Daniel Jenkinson, Geoffrey B. Jameson, Omid Qazvini, Lujia Liu, Andrew D. Burrows, Shane Telfer, and Christopher Richardson

Journal Name

RSCPublishing

ARTICLE

Interpenetration Isomers in Isoreticular Amine-tagged Zinc MOFs

Cite this: DOI: 10.1039/x0xx00000x

Received 00th January 2012,
Accepted 00th January 2012

DOI: 10.1039/x0xx00000x

www.rsc.org/

Afsaneh Khansari,[a] Macguire R. Bryant, [a] Daniel R. Jenkinson,[a] Geoffrey B. Jameson,[b] Omid T. Qazvini,[b] Lujia Liu,[c] Andrew D. Burrows,[d] Shane G. Telfer[b] and Christopher Richardson*[a]

The effect of increasing steric size of pendant amine substituents on structural isoreticulation has been studied systematically in a series of Zn-MOFs. Linear biphenyl dicarboxylic acids tagged with pendant primary amine (H_2bpdc-NH_2), allylamine (H_2bpdc-NHallyl), diallylamine (H_2bpdc-N(allyl)$_2$) and dimethylamine (H_2bpdc-NMe_2) groups react with zinc nitrate in DMF to yield a set of interpenetrated MOFs, **WUF-11-14**, respectively, that are structurally akin to IRMOF-9. The allylated amine ligands undergo C-N cleavage reactions under the synthesis conditions, yielding **WUF-12** and **WUF-13** as multivariate MOFs. The single crystal X-ray crystallography on this set of MOFs was not straightforward and we give a salutary account of the difficulties encountered. Gas adsorption measurements combined with surface area calculations provide invaluable support for the crystallographic assignments. The crystallographic analyses reveal subtle differences in the relative positions of the interpenetrating frameworks, and we present a classification system for this type of MOF and analyse related examples available in the literature. CO_2 adsorption measurements revealed that **WUF-14**, which features the strongest Brønsted basic dimethylamine tag group, has the highest capacity, isosteric heat of adsorption, and CO_2/N_2 selectivity.

Introduction

Amino groups are popular choices as functional tags for metal-organic frameworks (MOFs) because the framework topology of the parent MOF can often be replicated using the corresponding aryl amine ligand. This tactic has been used with the most widely investigated aryl amine ligand, 2-aminoterephthalic acid (H_2bdc-NH_2), to produce, *inter alia*, IRMOF-3,[1, 2] UiO-66-NH_2,[3] DMOF-1-NH_2,[4] UMCM-(3)1-NH_2,[4] MIL-53-NH_2,[5, 6] MIL-68(In)-NH_2,[7] MIL-101(Al)-NH_2,[8] and MIL-125-NH_2[9] frameworks by direct synthesis. The underlying motivation for making these materials is often to reap the beneficial effects that the amino functional groups have on the adsorption of CO_2. In addition, the incorporation of an amino group is often part of a strategy for post-synthetic modification (PSM), as they provide nucleophilic sites to subsequently introduce a wide variety of secondary functional groups.[10]

The longer congener, 2-amino-[1,1'-biphenyl]-4,4'-dicarboxylic acid (H_2bpdc-NH_2), has received less attention for both direct[11-19] and post-synthetic MOF syntheses.[20, 21] Also, there are only three reports of *N*-alkylated derivatives of H_2bpdc-NH_2.[22-24] The purpose of the present work is to detail the structural evolution of zinc(II) MOFs based on the nature of pendant amino substituents on a series of bpdc linkers. The four amino-functionalised linkers shown in Chart 1 were selected to delineate the impact of steric size and Brønsted basicity. Preparation of an isoreticular MOF series using these linkers would allow the role the functional group plays in the gas adsorption properties to become apparent. There are a limited number of similar studies in the literature.[2, 25-31] To probe the impacts of the tag groups, we examined CO_2 and N_2 adsorption properties.

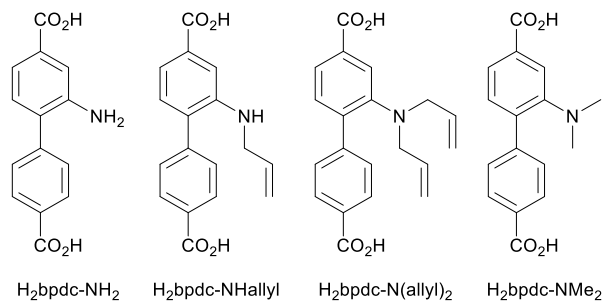

Chart 1 The structures of the amine-tagged biphenyldicarboxylate ligands.

Yaghi and co-workers noted that [1,1'-biphenyl]-4,4'-dicarboxylic acid (H_2bpdc) reacts with zinc(II) nitrate under dilute conditions in *N*,*N*-dimethylformamide (DMF) solvent to

give crystals with a single, non-interpenetrated $[Zn_4O(bpdc)_3]$ framework with a **pcu** topology (IRMOF-10).[1] Curiously, however, follow-up experimental studies on this MOF are rare. Under more concentrated conditions, crystals comprising doubly-interpenetrated **pcu** frameworks are readily formed (IRMOF-9).[1] Although control over interpenetration in a hydroxy-functionalised IRMOF-9/10 system has been demonstrated using special in-situ deprotection conditions,[32] a more common approach has been to suppress interpenetration on steric grounds by attaching sufficiently bulky pendant substituents to the biphenyl ligand backbone.[33-37] Kinetic and coordination modulation methods have also been shown to control interpenetration in other MOFs.[38, 39] It is also possible for bpdc-based zinc IRMOF networks to be partially interpenetrated wherein the second (interpenetrating) lattice is partially occupied.[40] In this light, the unambiguous assignment of the degree of interpenetration is crucial in the characterisation of IRMOF-9/10 framework analogues. Interpenetration has significant consequences for the positioning and the availability of the functional groups for interactions with guest molecules. Furthermore, the interpenetrating networks may be mutually disposed in various ways, which dictates the shape of the pore environment.

Experimental

Materials and methods

All chemicals used were of analytical grade and purchased from either Sigma Aldrich, VWR Australia or Ajax Finechem Pty Ltd. Synthetic and analytical details for H_2bpdc-NH_2, H_2bpdc-NHallyl, H_2bpdc-N(allyl)$_2$ and H_2bpdc-NMe_2 are given in the SI. ^{1}H NMR and ^{13}C NMR spectra were obtained using a Varian Mercury VX-300-MHz NMR spectrometer operating at 300 MHz for ^{1}H and 75.5 MHz for ^{13}C, a Bruker Ascend 400 MHz NMR spectrometer operating at 400 MHz for ^{1}H and 101 MHz for ^{13}C, or a Varian Inova-500-MHz NMR spectrometer, operating at 500 MHz for ^{1}H and 125 MHz for ^{13}C. ^{1}H NMR spectra were referenced to the residual *protio* peaks at 2.50 ppm in d_6-DMSO or 7.27 ppm in $CDCl_3$. ^{13}C NMR spectra were referenced to the solvent peaks at 39.6 ppm in d_6-DMSO or 77.7 ppm in $CDCl_3$. For ^{1}H NMR analysis, MOF samples (~10 mg) were digested by adding 35% DCl in D_2O (2 µL) and d_6-DMSO (500 µL) and stirring until a solution was obtained.

Simultaneous thermogravimetric and differential thermal analysis (TG-DTA) data were obtained using a Shimadzu DTG-60 instrument fitted with a FC-60A flow rate controller and TA-60WS thermal analyzer. Measuring parameters of 10 °C per min under nitrogen flow (20 cm^3 min^{-1}) were used. Powder X-ray diffraction (PXRD) patterns were recorded on a GBC-MMA X-ray diffractometer using Cu K(α) radiation (1.54180 Å) with samples mounted on 2.5 cm SiO_2 substrates. Experimental settings in the 2θ angle range of 3–30° of 0.02° step size and a scan speed of 1° min^{-1} were used. Gas adsorption studies were carried out using a Quantachrome Autosorb MP instrument and high purity nitrogen (99.999%) and carbon dioxide (99.995%) gases at the Wollongong Isotope Geochronology Laboratory. Surface areas were determined using Brunauer-Emmett-Teller (BET) calculations. Pore size distributions were calculated using the QSDFT kernel for N_2 at 77 K on carbon with slit/cylindrical pores as implemented in the Quantachrome software (v 3.0). The enthalpy of adsorption was calculated by fitting a virial equation to CO_2 isotherms measured at 273 K and 298 K. The Elemental Microanalysis Service at Macquarie University performed microanalyses using a PerkinElmer Elemental Analyzer, Model PE2400 CHNS/O. Each sample was heated at 110 °C for 2 h and analysed immediately afterward.

Single crystal X-ray diffraction (SCXRD) data were recorded on a Rigaku Spider diffractometer equipped with a MicroMax MM007 rotating anode generator (Cu radiation, 1.54180 Å), fitted with high flux Osmic multilayer mirror optics, and a curved image-plate detector. Data were collected at 292 K under d*TREK and were integrated and scaled and averaged with FS-Process.[41] XPREP was used to determine the space groups and the structures were solved using SHELXS and refined with SHELXL.[42] Details on the refinement can be found in the ESI to this article. Data are deposited with the Cambridge Structural Database (CCDC 1944583-1944586). Data can be obtained for free from www.ccdc.cam.ac.uk

Synthesis of IRMOF-9-NH_2 $[Zn_4O(bpdc\text{-}NH_2)_3]$, WUF-11 (WUF, Wollongong University Framework)

$Zn(NO_3)_2{\cdot}6H_2O$ (0.346 g, 1.16 mmol) and H_2bpdcNH_2 (0.100 g, 0.35 mmol) were dissolved in DMF (16 mL) and the solution was placed in an oven for 24 hours at 100 °C. The DMF solution was then exchanged for fresh DMF (2 × 2 mL) at 100 °C, then at room temperature for CH_2Cl_2 over 3 days, and then for benzene over 3 days. The sample was activated by freeze drying at –53 °C and 0.09 mbar for 1 hour followed by heating under dynamic vacuum at 120 °C for 5 hours. Yield 69.8 mg (57%). Anal. Calcd for $C_{42}H_{27}N_3O_{13}Zn_4$ | $[Zn_4O(bpdc\text{-}NH_2)_3]$: C, 48.35; H, 2.61; N, 4.03. Found: C, 48.17; H, 2.36; N, 3.62.

Synthesis and Data for WUF-12-14

Identical synthesis procedures to IRMOF-9-NH_2 were used for all other MOFs.

IRMOF-9-NHallyl (**WUF-12**): $Zn(NO_3)_2{\cdot}6H_2O$ (0.30 g, 1.0 mmol), H_2bpdc-NHallyl (0.100 g, 0.34 mmol). Yield 66.5 mg (47 %). Anal. Calcd for $C_{49.26}H_{44.68}N_3O_{17}Zn_4$ | $[Zn_4O(bpdc\text{-}NH_2)_{0.58}(bpdc\text{-}NHallyl)_{2.42}{\cdot}6H_2O]$: C, 47.38; H, 3.93; N, 3.37. Found: C, 47.24; H, 3.41; N, 3.62.

IRMOF-9-N(allyl)$_2$ (**WUF-13**): $Zn(NO_3)_2{\cdot}6H_2O$ (0.264 g, 0.887 mmol), H_2bpdc-N(allyl)$_2$ (0.100 g, 2.96 mmol). Yield 67.1 mg (53%). Anal. Calcd for $C_{52.62}H_{49.16}N_3O_{17}Zn_4$ | $[Zn_4O(bpdc\text{-}NHallyl)_{0.54}(bpdc\text{-}N(allyl)_2)_{2.46}{\cdot}3.5H_2O]$ C, 50.61; H, 3.89; N, 3.37. Found: C, 50.68; H, 3.36; N, 3.84.

IRMOF-9-NMe_2 (**WUF-14**): $Zn(NO_3)_2{\cdot}6H_2O$ (0.313 g, 1.05 mmol), H_2bpdc-NMe_2 (0.100 g, 0.35 mmol). Yield 69.5 mg (52%). Anal. Calcd for $C_{48}H_{45}N_3O_{16}Zn_4$ | $[Zn_4O(bpdc\text{-}NMe_2)_3{\cdot}3H_2O]$: C, 48.80; H, 3.84; N, 3.56. Found: C, 48.99; H, 3.29; N, 4.01.

Results and discussion

Syntheses of the ligands

H_2bpdc-NH_2 was prepared from Me_2bpdc-NO_2 by a convenient and high yielding hydrogenation procedure employing ammonium formate and Pd/C, producing Me_2bpdc-NH_2, followed by hydrolysis in aqueous hydroxide solution (see ESI). Each of the *N*-alkylated ligands were prepared in two-step syntheses starting from Me_2bpdc-NH_2 via reaction with allyl bromide or methyl iodide, as required, followed by ester cleavage in aqueous hydroxide solution (Scheme 1). Following careful acidification, the ligands were obtained as yellow powders in high yields and characterised by NMR spectroscopy, electrospray ionisation mass spectrometry (ESI-MS) and microanalysis (see ESI).

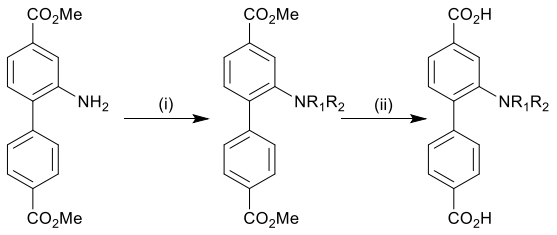

Scheme 1 Generalised synthetic pathway to the alkylated ligands. Reagents and conditions: (i) allyl bromide/methyl iodide, K_2CO_3/$NaHCO_3$, DMF, 70-90 °C (Me_2bpdc-NHallyl 57%; Me_2bpdc-N(allyl)$_2$ 85%, Me_2bpdc-NMe_2 73%); (ii) NaOH(aq), THF/MeOH, RT (H_2bpdc-NHallyl 97%; H_2bpdc-N(allyl)$_2$ 81%, H_2bpdc-NMe_2 87%).

Syntheses of the MOFs

MOF syntheses followed a well-established procedure of heating the functionalised bpdc linker with an excess of zinc(II) nitrate in DMF solvent at 100 °C. Using this procedure, IRMOF-9-NH_2 (**WUF-11**), IRMOF-9-NHallyl (**WUF-12**), IRMOF-9-N(allyl)$_2$ (**WUF-13**) and IRMOF-9-NMe_2 (**WUF-14**) were obtained as yellow or yellow-brown coloured crystals from H_2bpdc-NH_2, H_2bpdc-NHallyl, H_2bpdc-N(allyl)$_2$ and H_2bpdc-NMe_2, respectively. TG-DTA data for the as-synthesised samples (Fig. S9-S12) showed significant endothermic mass losses (47-62%) up to 240 °C, consistent with solvent being driven from the pores of the MOFs. The onset of exothermic decomposition of the frameworks was observed to start around 360 °C.

The as-synthesised MOFs were solvent exchanged with CH_2Cl_2 and dried before digestion in DCl/d_6-DMSO for analysis by ^{1}H NMR spectroscopy (Fig. S1-S4). The spectra show IRMOF-9-NH_2 and IRMOF-9-NMe_2 contain solely bpdc-NH_2 and bpdc-NMe_2 linkers, respectively; that is, the ligands have been incorporated in the frameworks without modification. However, IRMOF-9-NHallyl and IRMOF-9-N(allyl)$_2$ contain proportions of ligands that have been transformed during MOF synthesis. Specifically, *in situ* C-N bond cleavage occurs at nitrogen centres to expel some of the allyl groups. For example, IRMOF-9-NHallyl also contains bpdc-NH_2 bridging ligands (Fig. S2). Similarly, IRMOF-9-N(allyl)$_2$ contains bpdc-N(allyl)$_2$ and bpdc-NHallyl bridging ligands. This is clearly seen in the ^{1}H NMR spectrum of digested IRMOF-9-N(allyl)$_2$ by the presence of signals for the internal alkene of bpdc-N(allyl)$_2$ and bpdc-NHallyl around 5.6 and 5.8 ppm, respectively (Fig. S3). Small amounts of bpdc (~1-3%) were seen in some spectra resulting from cleavage of the C_{phenyl}-N bond rather than one of the C_{allyl}-N bonds. ESI-MS of digested MOF samples supported the C-N cleavage results (Fig. S5-S8). Therefore, IRMOF-9-NHallyl and IRMOF-9-N(allyl)$_2$ are multivariate MOFs.[43, 44] The ^{1}H NMR data were used to formulate the framework backbones of the MOFs (Table 1) and show that 18-19% of deallylated ligand is typically incorporated into **WUF-12** and **WUF-13** formed over 24 hours at 100 °C.

Curious as to the origin of the C-N cleavage observed during framework assembly, we carried out control experiments subjecting the respective methyl ester compounds to the conditions of MOF synthesis. No C-N cleavage was detected by ^{1}H NMR spectroscopy in this set of experiments. Some deallylation of the ester compounds was found, however, when benzoic acid was added to the reaction mixtures. This result suggests reactions of carboxylic acids, perhaps in forming zinc carboxylate clusters, may be responsible, and indicates the dicarboxylic acids play a crucial role in the deallylation phenomenon. ^{1}H NMR analysis of recovered organic material from the MOF syntheses revealed a similar constitution as that observed in the solids and indicates the deallylation reaction observed here occurs pre-incorporation to the MOF lattice. Syntheses of IRMOF-9-NHallyl and IRMOF-9-N(allyl)$_2$ were then performed at a lower temperature of 80 °C. Crystals started appearing in these reactions after 24 hours and the reactions were stopped at 48 hours. ^{1}H NMR spectroscopy on digested crystals surprisingly showed the proportion of deallylated ligands rose to 34% and 31%, respectively.

Table 1. Framework formulations determined by ^{1}H NMR spectroscopy in IRMOF-9-NHallyl and IRMOF-9-N(allyl)$_2$ synthesised at 80 °C and 100 °C.

	Synthesis Temp. (°C)	% bpdcNH$_2$	% bpdcNHallyl	% bpdcN(allyl)$_2$	Framework Formulation
IRMOF-9-NHallyl	100	19	81		[Zn$_4$O(bpdcNH$_2$)$_{0.58}$(bpdcNHallyl)$_{2.42}$]
IRMOF-9-NHallyl	80	34	66		[Zn$_4$O(bpdcNH$_2$)$_{1.2}$(bpdcNHallyl)$_{1.8}$]
IRMOF-9-N(allyl)$_2$	100		18	82	[Zn$_4$O(bpdcNHallyl)$_{0.54}$(bpdcN(allyl)$_2$)$_{2.46}$]
IRMOF-9-N(allyl)$_2$	80		31	69	[Zn$_4$O(bpdcNHallyl)$_{0.93}$(bpdcN(allyl)$_2$)$_{2.07}$]

In situ modification to ligands during framework synthesis are not uncommon, and have even being harnessed for control over ligand incorporation.[32, 45] Extensive C-N bond cleavage via *N*-demethylation of bdc-NMe$_2$ to bdc-NHMe has previously been observed during the synthesis of IRMOF (80%) and UiO-66 (63%) frameworks,[46] and the cleavage of a ligand C–C σ-bond has been observed in the synthesis of a zinc MOF.[47] Notably, we did not see any *N*-demethylation of bpdc-NMe$_2$ in this study (Fig. S4). As mentioned in the introduction, linkers substituted with amino groups represent an important class of MOF linkers, and these results point to an important consideration in the design and use of amino-functionalised ligands.

Structures of the MOFs

The structures of all as-synthesised MOFs were determined by single crystal X-ray diffraction (SCXRD). The analyses confirmed that, as expected, all frameworks are built up from Zn$_4$O nodes reticulated into cubic **pcu** networks by the linear dicarboxylate linkers, with a general formula of [Zn$_4$OL$_3$]. **WUF-11-14** are doubly-interpenetrated frameworks and are therefore functionalised analogues of IRMOF-9 ([Zn$_4$O(bpdc)$_3$]). Details of the crystallographic refinements can be found in the ESI.

The crystallography, however, was far from straightforward. Crystals of **WUF-11-13** are often highly twinned. The datasets of these crystals give E^2–1 values intermediate between those expected for centrosymmetric (0.968) and noncentrosymmetric (0.736) structures. These datasets could be successfully solved in the space group *P*-42$_1$*m* to give interpenetrated frameworks and refined using a twin model (either as a racemic twin or with a permutative twin matrix [010/001/100]). But, the datasets could also be successfully modeled in in alternative space groups. For example, **WUF-11** could be solved in *Pm*-3*m*, and **WUF-13** in *P*-4. The structures in these alternative space groups are noninterpenetrated i.e. at face value the datasets are compatible with both doubly interpenetrated or noninterpenetrated frameworks! Several observations, however, strongly suggested that the *P*-42$_1$*m* space group, and thus the doubly interpenetrated structures, were correct: (1) the observation of extinction under crossed polarisers precludes the cubic crystal system and thus the putative *Pm*-3*m* space group for **WUF-11**; (2) datasets on individual crystals that led to E^2–1 values around 0.9 had systematic absences that pointed to the *P*-42$_1$*m* space group; (3) datasets solved in the alternative space groups led to slightly poorer averaging and refinement statistics (most noticeably R_{int} and R_1) along with significant areas of residual electron density (large Q-peaks) in the framework pores. This electron density could not be successfully assigned to a coherent interpenetrating lattice even with a partial occupancy.

WUF-13 proved to be a particularly difficult case. This MOF was the most likely to be non-interpenetrated as it contains bpdc-N(allyl)$_2$ ligands with the largest steric demand. Crystals of as-synthesized **WUF-13** have the propensity to form as large intergrown crystals that display non-uniform extinction properties, with regions that extinguished polarised light as well as regions that did not, perhaps indicating a delicate balance for interpenetration in this system. A dramatic improvement in optical properties was achieved by solvothermal annealing these crystals at 85 °C in fresh dry DMF for 48 hours. The size of the crystals was followed in this process and typically showed small size reductions of ~2-4% along the two crystal dimensions measured (Fig. S22 and Table S3). This value is very much smaller than is required to convert from a non-interpenetrated to fully interpenetrated phase (25%) via an autocatenation process.[48] SCXRD analysis on crystals post annealing did, however, show much better diffraction and consistently returned the interpenetrated structure.

The salutary lesson here is that had all twin domains been on the nanoscale, then in all likelihood, extinction and hence twinning would not have been detected. The apparent (non-interpenetrated) SCXRD structures would have been at odds with the gas adsorption data (see **Gas adsorption studies**), which indicates a void volume very much smaller than a noninterpenetrated structure. These datasets serve as a cautionary example for the sole use of SCXRD in distinguishing interpenetrated from non-interpenetrated IRMOF-9-type frameworks. While this distinction is unequivocal in many cases, turning a blind eye to extinction properties under crossed polarisers and poor refinement statistics, may easily have led to the misassignment of interpenetration in some circumstances. The risk would be further exacerbated by the use of crystallographic tools that eliminate residual electron density (such as SQUEEZE in PLATON).

Structural differences exist within this set of interpenetrated structures. By virtue of IRMOF-9-NH$_2$, -NHallyl and -N(allyl)$_2$, crystallising in the *P*-42$_1$*m* space group they share the same positioning between the interpenetrated networks (Fig. 1a, b; ESI Movie 1). In this arrangement, the SBU of the second framework

is situated centrally near one of the square faces of the host framework (Fig. 1b). This arrangement results in closest contacts between the interpenetrated networks occurring around the midpoints of the biphenyl linkers (ca. 3.8 Å between closest phenyl ring carbons). This region is where the amino tag groups reside; however, these groups were not located in difference maps, presumably because of four-site disorder. They were placed in representative sites to complete the crystallographic models and held fixed during structure refinement. The tag groups were implanted at full occupancy so the contributions from the minor dicarboxylates in the multivariate MOFs **WUF-12** and **WUF-13** was not accounted for in the refinements. Rectangular (~15×7 Å) and square (~8×8 Å) pores are observable along the [010] and [001] directions, respectively (Fig. 1a, b), but the largest pore system in this arrangement (~10×10 Å) runs parallel to the [110] direction.

The arrangement of the interpenetrated networks in IRMOF-9-NMe_2 (**WUF-14**) is different. This MOF crystallises in the centrosymmetric space group *R*-3*m* with Zn_4O SBUs of interpenetrating networks related by crystallographic inversion. This arrangement results in positioning the SBU of the second network deeper into the pore bounded by the two networks (Fig. 1c, d; SI Movie 2), rather than near a square face. This results in pores of ~12×14 Å penetrating the crystal lattice along the [211] and [122] directions. Another much smaller pore of ~3 Å exists along the [001] direction. The nitrogen atom of the dimethylamine functional group was located in the difference map but the attached methyl groups were not and these were placed in geometrically reasonable positions and refined with fixed bond lengths and angles.

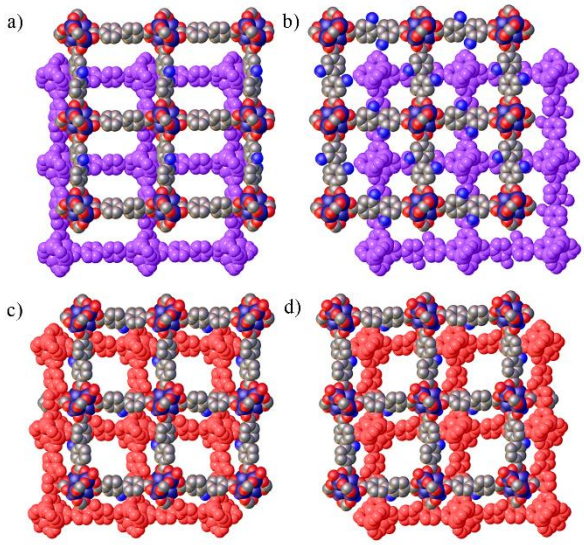

Fig. 1 Orthogonal views of the interpenetration arrangement for IRMOF-9-NH_2 (**WUF-11**), IRMOF-9-NHallyl (**WUF-12**) and IRMOF-9-N(allyl)$_2$ (**WUF-13**) along a) the b-axis and b) the c-axis; c) and d) orthogonal views for IRMOF-9-NMe_2 (**WUF-14**). Carbon atoms of tag groups and all hydrogen atoms are not shown for clarity

The interpenetration arrangements observed here and in other examples from our labs[49-53] prompted us to classify the modes of interpenetration observed in IRMOF-9 and functionalised analogues, as determined by SCXRD (Table S2). Three situations for interpenetration are observed (Figure 2). We define Type I as having a SBU located precisely at the centre of the cuboid defined by the host framework and therefore equidistant from all host vertices. Type II has the SBU equidistant from four of the host vertices and can exist from the body centre of the host framework toward the centre of one of the host framework faces. It cannot exist in the face-centred position because of steric clashes with bridging ligands of the host framework. Type III is where the SBU is closest to only one host vertex. Our analysis shows 17 of the 26 interpenetrated IRMOF-9-type structures analysed crystallise as Type III. This arrangement is possible with linker substituents that allow the frameworks to approach closely to maximise noncovalent interactions. There are far fewer frameworks that crystallise in Type II, but this arrangement is observed in three out of the four structures reported here. Although this relative positioning relaxes non covalent interactions between bridging ligands, it provides greater opportunity for larger substituents to point to the central cavity and less chance of encountering steric clashing. This suggests Type II is more suited to larger substituents, such as NHallyl and -N(allyl)$_2$ found in **WUF-12** and **WUF-13**. Only one system we are aware of crystallises in Type I. This unique system containing bulky phenyl-substituted diazocine substituents allows complementary π-π contacts between the ligands on each framework when the second SBU is located precisely at the centre of the host lattice.

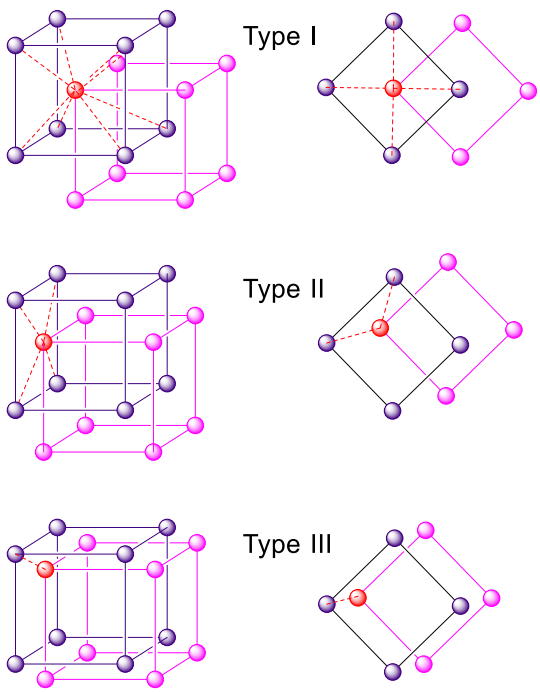

Fig. 2 Perspective and top-down views of the interpenetration Types in IRMOF-9-type structures.

Gas adsorption studies

Figure 3 shows the N_2 isotherms for the MOFs at 77 K, and Table 2 summarises the surface area and pore volume data from

measurements and calculations. Individual adsorption-desorption isotherms are provided in Fig. S28-S31. Each sample shows a Type I isotherm typical of microporous MOF materials. IRMOF-9-NH_2 with the smallest primary amine tag group has the highest apparent BET surface area of 2262 m^2g^{-1}, and this compares well with the calculated surface area of 2522 m^2g^{-1}. **WUF-12** has an apparent surface area (2095 m^2g^{-1}) that is higher than that calculated (1736 m^2g^{-1}). This is explained by the calculation model requiring full occupancy NHallyl tags, where the true material has ~19% of these groups cleaved during synthesis to smaller and lighter primary amine groups. **WUF-13**, with the largest diallyl amine functional group, also has a higher apparent surface area (1600 m^2g^{-1}) than that calculated (1253 m^2g^{-1}) and this is again explained by deallylation. IRMOF-9-NHallyl and IRMOF-9-N(allyl)$_2$ synthesised at 80 °C have equivalent or higher surface areas (2002 m^2g^{-1} and 1787 m^2g^{-1}, respectively) than that synthesised at 100 °C, consistent with that expected based on a greater proportion of deallylated linkers (34% and 31%, respectively). The apparent surface area of IRMOF-9-NMe_2 is 1683 m^2g^{-1} (calc. 2177 m^2g^{-1}). The activation of this MOF was particularly difficult. After extensive effort, the best method was supercritical CO_2 drying of the MOF from a benzene solution. Notably, the SCXRD analysis showed this MOF had a water molecule bound to each framework node, and the electron density within the cage-like pore that forms between framework nodes (ESI Movie 3) was modelled as water molecules. We ascribe the difficulties of activating this MOF to successfully removing these water molecules to the presence of and attraction to the -NMe_2 groups that line the cage windows.

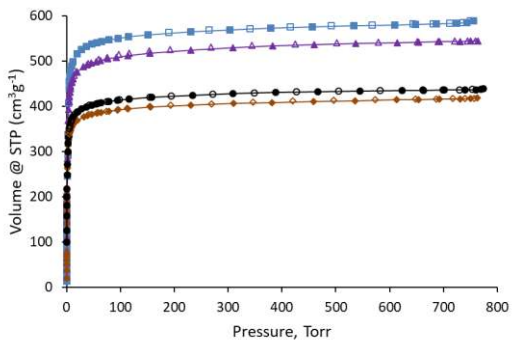

Fig 3. Nitrogen gas adsorption-desorption isotherms at 77 K for IRMOF-9-NH_2 (blue), IRMOF-9-NHallyl (purple), IRMOF-9-N(allyl)$_2$ (brown) and IRMOF-9-NMe_2 (black). Closed symbols adsorption, open symbols desorption.

The pore size distributions of the MOFs were modelled by DFT calculations. The results show the distributions narrow with increasing size of the amino substituent, consistent with pore constriction by larger functional groups (IRMOF-9-NH_2, 7.5-14 Å; IRMOF-9-NHallyl, 8.5-12 Å; IRMOF-9-N(allyl)$_2$, 8.5-11 Å) (Fig. S32). These results are in fair agreement with dimensions from SCXRD when considering van der Waals radii. IRMOF-9-NMe_2 shows a distribution tightly clustered between 8 and 11 Å. This is smaller than the dimensions obtained from the SCXRD analyses (~12×14 Å); however, it should be borne in mind that gas adsorption data were recorded at 77 K on activated samples while the SCRXD data were collected at 292 K on solvated samples. This trend is mirrored in the data for the corresponding pore volumes shown in Table 2, which decrease across the series.

Table 2. Apparent surface areas, pore volumes, isosteric heats of adsorption and CO_2/N_2 selectivity's for the MOFs.

Structure	SA (m^2g^{-1})[a] (calc)	Pore Volume (cm^3g^{-1})[b] N_2 (CO_2)	Q^0_{st} CO_2 ($kJmol^{-1}$)[c]	CO_2 / N_2 Selectivity[d]
IRMOF-9-NH_2	2262 (2522)	0.90 (0.95)	17.5	12.5
IRMOF-9-NHallyl	2095 (1736)	0.84 (0.87)	19	9.5
IRMOF-9-N(allyl)$_2$	1600 (1253)	0.64 (0.67)	20	10.0
IRMOF-9-NMe_2	1683 (2177)	0.67 (0.66)	28	15.1

[a] Apparent surface area from BET analysis for N_2 at 77 K. [b] At P/P_0 0.90 for N_2 at 77 K and at 520 torr for CO_2 at 196 K. [c] From virial fitting calculations. [d] Selectivity from IAST calculations (15% CO_2 and 85% N_2 at 298 K).

We became interested in the effects of desolvation on the Type II MOFs hypothesising that, to achieve greater stabilisation during desolvation, the networks might move relative to the positions determined from the solvated crystal structures. Calculations coupled with SCXRD analyses indicate IRMOF-9 may have considerable plasticity.[54] We pursued this by measuring the dimensions of crystals of as-synthesised samples as they dried under ambient conditions over 48 hours. IRMOF-9-NH_2 and IRMOF-9-N(allyl)$_2$ were selected for this part of the study as the MOFs containing the smallest and largest substituents. The measurements are presented in Table S4-S5 and shown in graphical form in Fig. S23-S24 and S26-S27. Crystals of IRMOF-9-NH_2 show size reductions along edge dimensions of ~18-22% over 48 hours with most of the size reduction occurring in the first hour (~10-12%). The size reductions for IRMOF-9-N(allyl)$_2$ also occur over the first hours but are typically smaller in magnitude (~8-12% over the first hour and ~13-18% over 48 hours). ^{1}H NMR analysis showed the change in size is congruent with the loss of DMF solvent from the frameworks. After 48 hours, the number of DMF molecules reduced from eight to three and from six to three per formula unit for IRMOF-9-NH_2 and IRMOF-9-N(allyl)$_2$, respectively. The optical micrographs show crystal morphology is retained during desolvation (see Fig. S25 for an example) yet PXRD studies showed that neither MOF retains sufficient long-range order to give diffraction after more than half an hour in the air. This thwarted further study of the materials by PXRD.

Considering this set of MOFs functionalised with amino tag groups, we were interested in observing their performance in the adsorption of CO_2. The CO_2 sorption data at 196 K (Fig. S33-S38) show that equivalent uptake were obtained compared to the N_2 data at 77 K and corresponding pore volumes were obtained (Table 2). Full adsorption-desorption isotherms recorded from 273 K to 298 K are shown in Fig. S39-S47. The CO_2 adsorption data at 298 K displayed in Fig. 4 is typical of the order observed in the series with IRMOF-9-NMe_2 > IRMOF-9-NHallyl > IRMOF-9-N(allyl)$_2$ > IRMOF-9-NH_2. The uptake capacities

between 273 K and 298 K are summarised in Table S6 and show IRMOF-9-NMe_2 has the highest uptake at 1 bar with 55 cm^3g^{-1} at 273 K and 31 cm^3g^{-1} at 298 K whereas IRMOF-9-NH_2 displayed the lowest CO_2 uptake with 41 cm^3g^{-1} at 273 K and 23 cm^3g^{-1} at 298 K, despite possessing the highest surface area from N_2 measurements at 77 K. Our measurements agree well with previous GCMC simulations of CO_2 uptake for the IRMOF-9-NH_2 framework.[55]

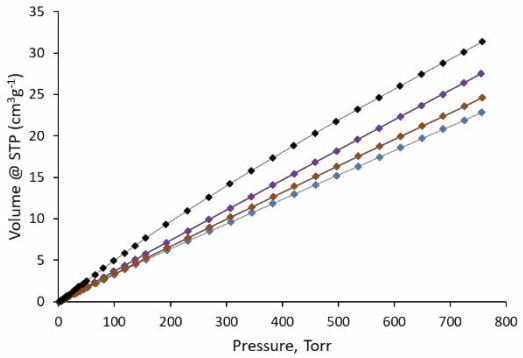

Fig. 4 CO_2 adsorption isotherms recorded at 298 K for IRMOF-9-NH_2 (blue), IRMOF-9-NHallyl (purple), IRMOF-9-N(allyl)$_2$ (brown) and IRMOF-9-NMe_2 (black).

The selectivity of CO_2/N_2 adsorption was determined by IAST calculations from single-component CO_2 and N_2 isotherms from a theoretical gas mixture consisting of 15 mol% CO_2 and 85 mol% N_2 and is displayed graphically in Fig. S48-S51. The best performing material is again IRMOF-9-NMe_2 with a selectivity of 15.1 and with slightly better performance at 298 K than 273 K. In contrast, IRMOF-9-N(allyl)$_2$, which also contains a tertiary amine group, shows a relatively poorer performance, with a selectivity of 10.0 at 298 K. IRMOF-9-NHallyl performs similarly to IRMOF-9-N(allyl)$_2$ although with a slightly lower selectivity of 9.5 while IRMOF-9-NH_2 has a selectivity factor of 12.5 at 298 K.

Recognising the interplay between amine nucleophilicity, basicity and steric profile we sought to probe the strength of the CO_2-framework interaction by calculating Q_{st} values. Fig. 5 shows the results of virial fitting the CO_2 data at 273 K and 298 K for each of the MOFs.

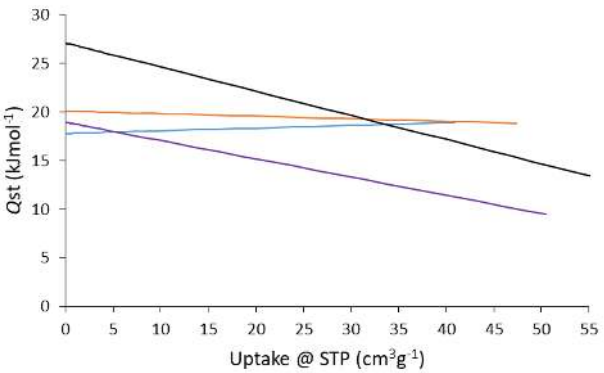

Fig. 5 A plot of the isosteric heats of adsorption of CO_2 for IRMOF-9-NH_2 (blue), IRMOF-9-NHallyl (purple), IRMOF-9-N(allyl)$_2$ (brown) and IRMOF-9-NMe_2 (black).

The values indicate rather weak physisorption of CO_2 to the frameworks. The tertiary amine MOFs, IRMOF-9-NMe_2 and IRMOF-9-N(allyl)$_2$, have the highest heats of adsorption. However, the Q_{st} profile for IRMOF-9-NMe_2 reduces comparatively steeply from 27 kJ/mol at low uptake to ~14 kJ/mol at 55 cm^3g^{-1} whereas IRMOF-N(allyl)$_2$ maintains a Q_{st} around 20 kJ/mol out to near 50 cm^3g^{-1}. The profile of IRMOF-9-NHallyl also reduces quite steeply while IRMOF-9-NH_2 starts at 17.5 kJ/mol and shows a very small upward trend. In general, the Q_{st} at low coverage follows the same order as the aqueous basicity of the amine: -NMe_2 > -N(allyl)$_2$ > -NHallyl > -NH_2. As IRMOF-9-NH_2, -NHallyl and -N(allyl)$_2$ share the same network arrangement, changes in enthalpy of adsorption can be rationalised based on decreasing pore size and increasing amine basicity across these three MOFs. The orientation and availability of the functional groups in the pore environment is also a prime consideration but unfortunately could not be precisely determined by the SCXRD experiments.

In previous work, the enthalpy of adsorption in functionalised IRMOF-9-type compounds was attributed primarily to pore size.[55] Each of the functionalised IRMOF-9s studied crystallised in Type III with a larger open pore and an inaccessible small pore blocked off by the pendant tag groups, negating effective interaction with CO_2. Although this arrangement is seen here for IRMOF-9-NMe_2 the very strongly basic dimethylamino group leads to a higher enthalpy of adsorption compared to IRMOF-9 despite possessing a larger pore size.

Conclusions

Four interpenetrated amine-containing analogues of IRMOF-9 have been prepared and fully characterised. The dealkylation of secondary and tertiary amines in the solvothermal preparation of the zinc MOFs containing *N*-allyl groups adds to previous observations and suggests this may be a general phenomenon.

The crystal structures of functionalised IRMOF-9 compounds can be classified into three types. Most crystallise with solvent-filled pores as Type III, which offers close inter-framework interactions and one open pore system. The amino-functionalised IRMOF-9-NH_2, IRMOF-9-NHallyl and IRMOF-9-N(allyl)$_2$ compounds synthesised here crystallise as Type II. This results in close contacts around the inter-ring areas of the biphenyl ligands and leads to multiple types of channels. IRMOF-9-NH_2 and IRMOF-9-N(allyl)$_2$ show considerable plasticity, as demonstrated by simple desolvation studies. Releasing the full potential of interpenetrated frameworks is likely to come from understanding and harnessing such dynamic behaviour.

In terms of CO_2 adsorption, IRMOF-9-NMe_2 and IRMOF-9-N(allyl)$_2$ showed the most interesting results. These MOFs contain polar tertiary amines and have smaller pores, indicating electrostatics play a defining role for these systems. The highest CO_2 uptake and selectivity was achieved with the MOF containing the best Brønsted base amongst the functional groups, IRMOF-9-NMe_2.

Conflicts of interest

There are no conflicts of interest to declare.

Acknowledgements

CR gratefully acknowledges the University of Wollongong for financial support. SGT thanks the MacDiarmid Institute and the RSNZ Marsden Fund for funding. This research is supported by Australian Government Research Training Program (RTP) Scholarships to AK and MRB.

Notes and references

[a] School of Chemistry and Molecular Bioscience, University of Wollongong, Wollongong NSW 2522, Australia; Tel:+ 61 2 4221 3254; E-mail: chris_richardson@uow.edu.au.

[b] MacDiarmid Institute for Advanced Materials and Nanotechnology, Institute of Fundamental Sciences, Massey University, Palmerston North, New Zealand.

[c] Department of Chemistry, Northwestern University, 2145 Sheridan Road, Evanston, Illinois 60208-3113, United States.

[d] Department of Chemistry, University of Bath, Claverton Down, Bath BA2 7AY, UK.

Electronic Supplementary Information (ESI) available: Synthetic procedures, TG–DTA data, descriptions of asymmetric units and additional SCXRD data, ^{1}H NMR digestion spectra, gas sorption isotherms, virial fitting parameters, IAST plots. See DOI: 10.1039/b000000x/

1. D. Vodak, M. Eddaoudi, J. Kim, N. Rosi, J. Wachter, M. O'Keeffe and O. M. Yaghi, *Science*, 2002, **295**, 469-472.
2. J. L. C. Rowsell and O. M. Yaghi, *J. Am. Chem. Soc.*, 2006, **128**, 1304-1315.
3. F. Vermoortele, R. Ameloot, A. Vimont, C. Serre and D. De Vos, *Chem. Commun.*, 2011, **47**, 1521-1523.
4. Z. Wang, K. K. Tanabe and S. M. Cohen, *Inorg. Chem.*, 2009, **48**, 296-306.
5. S. Bauer, C. Serre, T. Devic, P. Horcajada, J. Marrot, G. Férey and N. Stock, *Inorg. Chem.*, 2008, **47**, 7568-7576.
6. T. Ahnfeldt, N. Guillou, D. Gunzelmann, I. Margiolaki, T. Loiseau, G. Férey, J. Senker and N. Stock, *Angew. Chem. Int. Ed.*, 2009, **48**, 5163-5166.
7. M. Savonnet, E. Kockrick, A. Camarata, D. Bazer-Bachi, N. Bats, V. Lecocq, C. Pinel and D. Farrusseng, *New J. Chem.*, 2011, **35**, 1892-1897.
8. P. Serra-Crespo, E. V. Ramos-Fernandez, J. Gascon and F. Kapteijn, *Chem. Mater.*, 2011, **23**, 2565-2572.
9. M. A. Moreira, J. C. Santos, A. F. P. Ferreira, J. M. Loureiro, F. Ragon, P. Horcajada, P. G. Yot, C. Serre and A. E. Rodrigues, *Langmuir*, 2012, **28**, 3494-3502.
10. Z. Wang and S. M. Cohen, *Chem. Soc. Rev.*, 2009, **38**, 1315-1329.
11. J. E. Halls, A. Hernan-Gomez, A. D. Burrows and F. Marken, *Dalton Trans.*, 2012, **41**, 1475-1480.
12. A. M. Rasero-Almansa, A. Corma, M. Iglesias and F. Sanchez, *ChemCatChem*, 2014, **6**, 3426-3433.
13. X. Xu, J. A. van Bokhoven and M. Ranocchiari, *ChemCatChem*, 2014, **6**, 1887-1891.
14. M. A. Gotthardt, S. Grosjean, T. S. Brunner, J. Kotzel, A. M. Gaenzler, S. Wolf, S. Braese and W. Kleist, *Dalton Trans.*, 2015, **44**, 16802-16809.
15. S. Halis, N. Reimer, A. Klinkebiel, U. Luening and N. Stock, *Microporous Mesoporous Mater.*, 2015, **216**, 13-19.
16. M. Kaposi, M. Cokoja, C. H. Hutterer, S. A. Hauser, T. Kaposi, F. Klappenberger, A. Poethig, J. V. Barth, W. A. Herrmann and F. E. Kuehn, *Dalton Trans.*, 2015, **44**, 15976-15983.
17. R. Sun, B. Liu, B.-G. Li and S. Jie, *ChemCatChem*, 2016, **8**, 3261-3271.
18. N. P. Martin, J. Marz, H. Feuchter, S. Duval, P. Roussel, N. Henry, A. Ikeda-Ohno, T. Loiseau and C. Volkringer, *Chem. Commun.*, 2018, **54**, 6979-6982.
19. T.-Y. Luo, C. Liu, X. Y. Gan, P. F. Muldoon, N. A. Diemler, J. E. Millstone and N. L. Rosi, *J. Am. Chem. Soc.*, 2019, **141**, 2161-2168.
20. C. Liu, T.-Y. Luo, E. S. Feura, C. Zhang and N. L. Rosi, *J. Am. Chem. Soc.*, 2015, **137**, 10508-10511.
21. C.-X. Chen, Z.-W. Wei, J.-J. Jiang, S.-P. Zheng, H.-P. Wang, Q.-F. Qiu, C.-C. Cao, D. Fenske and C.-Y. Su, *J. Am. Chem. Soc.*, 2017, **139**, 6034-6037.
22. M. J. Katz, S.-Y. Moon, J. E. Mondloch, M. H. Beyzavi, C. J. Stephenson, J. T. Hupp and O. K. Farha, *Chem. Sci.*, 2015, **6**, 2286-2291.
23. S.-Y. Moon, G. W. Wagner, J. E. Mondloch, G. W. Peterson, J. B. DeCoste, J. T. Hupp and O. K. Farha, *Inorg. Chem.*, 2015, **54**, 10829-10833.
24. G. W. Peterson, S.-Y. Moon, G. W. Wagner, M. G. Hall, J. B. De Coste, J. T. Hupp and O. K. Farha, *Inorg. Chem.*, 2015, **54**, 9684-9686.
25. M. Kandiah, M. H. Nilsen, S. Usseglio, S. Jakobsen, U. Olsbye, M. Tilset, C. Larabi, E. A. Quadrelli, F. Bonino and K. P. Lillerud, *Chem. Mater.*, 2010, **22**, 6632-6640.
26. S. T. Meek, J. J. Perry, S. L. Teich-Mcgoldrick, J. A. Greathouse and M. D. Allendorf, *Cryst. Growth Des.*, 2011, **11**, 4309-4312.
27. Y. Huang, W. Qin, Z. Li and Y. Li, *Dalton Trans.*, 2012, **41**, 9283-9285.
28. L. Liu, K. Konstas, M. R. Hill and S. G. Telfer, *J. Am. Chem. Soc.*, 2013, **135**, 17731-17734.
29. H. Furukawa, F. Gándara, Y.-B. Zhang, J. Jiang, W. L. Queen, M. R. Hudson and O. M. Yaghi, *J. Am. Chem. Soc.*, 2014, **136**, 4369-4381.
30. L. Liu and S. G. Telfer, *J. Am. Chem. Soc.*, 2015, **137**, 3901-3909.
31. D. C. Young, H. Yang, S. G. Telfer and P. E. Kruger, *Inorg. Chem.*, 2017, **56**, 12224-12231.
32. D. Rankine, A. Avellaneda, M. R. Hill, C. J. Doonan and C. J. Sumby, *Chem. Commun.*, 2012, **48**, 10328-10330.
33. R. K. Deshpande, J. L. Minnaar and S. G. Telfer, *Angew. Chemie Int. Ed.*, 2010, **49**, 4598-4602.
34. A. Sen Gupta, R. K. Deshpande, L. Liu, G. I. N. Waterhouse and S. G. Telfer, *CrystEngComm*, 2012, **14**, 5701-5704.
35. J. M. Roberts, O. K. Farha, A. A. Sarjeant, J. T. Hupp and K. A. Scheidt, *Cryst. Growth Des.*, 2011, **11**, 4747-4750.
36. T.-H. Park, K. Koh, A. G. Wong-Foy and A. J. Matzger, *Cryst. Growth Des.*, 2011, **11**, 2059-2063.
37. R. K. Deshpande, G. I. Waterhouse, G. B. Jameson and S. G. Telfer, *Chem. Commun.*, 2012, **48**, 1574-1576.
38. R. J. Marshall, C. T. Lennon, A. Tao, H. M. Senn, C. Wilson, D. Fairen-Jimenez and R. S. Forgan, *J. Mater. Chem. A*, 2018, **6**, 1181-1187.
39. D. Bara, C. Wilson, M. Mörtel, M. M. Khusniyarov, S. Ling, B. Slater, S. Sproules and R. S. Forgan, *J. Am. Chem. Soc.*, 2019, **141**, 8346-8357.
40. A. Ferguson, L. Liu, S. J. Tapperwijn, D. Perl, F.-X. Coudert, S. Van Cleuvenbergen, T. Verbiest, M. A. van der Veen and S. G. Telfer, *Nat. Chem.*, 2016, **8**, 250-257.
41. J. Rigaku Corporation: Tokyo, *Journal*, 1996.
42. G. M. Sheldrick, *Acta Cryst. A*, 2008, **A64**, 112-122.
43. H. Deng, C. J. Doonan, H. Furukawa, R. B. Ferreira, J. Towne, C. B. Knobler, B. Wang and O. M. Yaghi, *Science*, 2010, **327**, 846-850.
44. A. D. Burrows, *CrystEngComm*, 2011, **13**, 3623-3642.
45. H. Kitagawa and T. Yamada, *J. Am. Chem. Soc.*, 2009, **131**, 6312-6312.
46. H. Hahm, H. Ha, S. Kim, B. Jung, M. H. Park, Y. Kim, J. Heo and M. Kim, *CrystEngComm*, 2015, **17**, 5644-5650.
47. B. Liu, H.-F. Zhou, Z.-H. Guan, L. Hou, B. Cui and Y.-Y. Wang, *Green Chem.*, 2016, **18**, 5418-5422.
48. A. Ferguson, L. Liu, S. J. Tapperwijn, D. Perl, F. X. Coudert, S. Van Cleuvenbergen, T. Verbiest, M. A. van der Veen and S. G. Telfer, *Nat. Chem.*, 2016, **8**, 250-257.

49. A. D. Burrows, C. Frost, M. F. Mahon and C. Richardson, *Angew. Chem. Int. Ed.*, 2008, **47**, 8482-8486.
50. A. D. Burrows, C. G. Frost, M. F. Mahon and C. Richardson, *Chem. Commun.*, 2009, DOI: 10.1039/b906170c, 4218-4220.
51. A. D. Burrows, S. O. Hunter, M. F. Mahon and C. Richardson, *Chem. Commun.*, 2013, **49**, 990-992.
52. M. R. Bryant, A. D. Burrows, C. J. Kepert, P. D. Southon, O. T. Qazvini, S. G. Telfer and C. Richardson, *Cryst. Growth Des.*, 2017, **17**, 2016-2023.
53. M. R. Bryant, T. A. Ablott, S. G. Telfer, L. Liu and C. Richardson, *CrystEngComm*, 2019, **21**, 60-64.
54. S. Canossa, P. Pelagatti and A. Bacchi, *Isr. J. Chem.*, 2018, **58**, 1131 – 1137.
55. R. Babarao, C. J. Coghlan, D. Rankine, W. M. Bloch, G. K. Gransbury, H. Sato, S. Kitagawa, C. J. Sumby, M. R. Hill and C. J. Doonan, *Chem. Commun.*, 2014, **50**, 3238-3241.